ADVANCED ENERGY MATERIALS
www.advenergymat.de

Determining the Effectiveness of Radiative Cooler-Integrated Solar Cells

Se-Yeon Heo, Do Hyeon Kim, Young Min Song, and Gil Ju Lee**

The power-conversion efficiency of solar cells (SCs) is reduced at high temperatures. A radiative cooling process can be implemented to overcome this issue. The radiative cooler (RC) presents considerable potential in the design of an ideal broadband emitter, which emits heat through the entire atmospheric transmittance window for devices with operating temperatures that significantly exceed the ambient temperature. However, the performance of these devices varies based on the type of SCs. This study aims to determine the dependency of the radiative cooling power for various types of SCs and proposes the multi-junction SC (MJSC), which is the SC that benefits the most from RCs. The integrated cooler is designed with a micro-grating which can enhance the emissivity within entire atmospheric transmittance window and can also lead to the light-trapping aspect in the solar spectrum. Outdoor field tests demonstrate both the enhanced cooling performance and the power conversion efficiency of the proposed MJSC when compared to a conventional glass-mounted MJSC under direct sunlight of ≈900 Wm^{-2} including a temperature drop of ≈6 °C and minimization of the variation of the open-circuit voltage to ≈6%. Future research is expected to develop a theoretical bridge between the field of SCs and radiative cooling.

1. Introduction

Extensive research has been conducted in recent years to increase the power conversion efficiency of solar cells (SCs).[1,2] A previous study proposed the improvement of intrinsic efficiency beyond the Shockley–Queisser (SQ) limits, by steering different wavelength bands of sunlight toward an SC using a multi-junction design.[3–5] The efficiency of SCs can be further improved by enhancing the light absorption using light-trapping techniques, which include geometrical engineering of the SC, and the application of grating,[6,7] random,[8,9] and plasmonic[10–13] structures. However, an SC cannot practically achieve this efficiency due to its dependency on the operating temperature. It is stated that the high efficiency in various SCs can be achieved at an illumination of AM 1.5G and a temperature of 25 °C. However, the temperature of the SC typically exceeds this value in outdoor conditions, where it heats up by tens of degrees above the ambient temperature, which decreases the lifespan and efficiency of the SC.[14,15]

The passive radiative cooling method can potentially resolve the heating issue of the SC owing to its compact and cost-effective approach. It involves spontaneously cooling objects by emitting heat to the outer space without consuming energy through the transparent atmospheric transmittance window ($\lambda \approx 8$–13 μm).[16–18] Recent studies have presented various types of radiative coolers (RCs)[19–27] which have been demonstrated to successfully lower the temperature of SCs.[28–30] Research has also been conducted to theoretically analyze the effectiveness of RCs in compensating for the reduced conversion efficiency of SCs due to elevated temperatures.[31–34] However, these studies have evaluated or tested the potential of an RC on specific target SCs, such as silicon,[35–39] concentrated perovskite,[40–43] or low-bandgap concentrated perovskite,[41] which are limited to single-junction SCs. Further research is required to determine the type of SC that can most retain its original efficiency even at high environmental temperatures, when adapting the RC technique.

The efficiency of SCs can be significantly improved through a comprehensive understanding of the practical operation of the RC on diverse SCs since the SC industry encompasses various types of cells. This study theoretically proves that the multi-junction SC (MJSC) is the most effective type of SC when an RC is applied. It also presents the limitations of the radiative cooling technique when sub-bandgap (sub-BG) absorption is considered. Consequently, the proposed MJSC is demonstrated to be immune to heating by sub-BG photons, which can lead to the development of novel SCs by reducing the burden of designing additional sub-BG filters[44] or reflectors.[45–47] A structure is then fabricated which performs both light trapping and radiative cooling based on pioneering SC research, and is applied to the InGaP/GaAs/Ge MJSC. Multiple outdoor experiments are conducted to demonstrate that radiative cooling can contribute to a temperature drop of ≈6 °C. The reduced temperature also results in an absolute increase of the open-circuit

S.-Y. Heo, D. H. Kim, Y. M. Song
School of Electrical Engineering and Computer Science (EECS)
Gwangju Institute of Science and Technology (GIST)
Gwangju 61005, Republic of Korea
E-mail: ymsong@gist.ac.kr
G. J. Lee
Department of Electronics Engineering
Pusan National University
Busan 46241, Republic of Korea
E-mail: gjlee0414@pusan.ac.kr

The ORCID identification number(s) for the author(s) of this article can be found under https://doi.org/10.1002/aenm.202103258.

DOI: 10.1002/aenm.202103258

voltage of the MJSC by ≈2%. Therefore, RCs are expected to be closely connected to the next generation of efficiency control methods through precise prediction in modeling SCs which are immune to heat from the external environment, thus reducing the design complexity.

2. Theoretical Framework for RC Coupled with SC System

Typically, an SC is an energy converter that turns solar energy into electricity. Even ideal SC, there are energy losses related to the spectral mismatch between the incident solar radiation and the absorption in the SC: photons have lower energy than bandgap (P_{sub-BG}) are not absorbed and photons have higher energy than the bandgap ($P_{above-BG}$) are not fully converted to electrical energy due to thermalization and the rest is converted into heat.[3] To manage the heat and realize the full potential of SC, a module that RC integrated with SC is suggested in **Figure 1**a. The ideal module i) fully absorbs the $P_{above-BG}$, ii) fully reflects P_{sub-BG}, and iii) fully emits heat at longer wavelengths. The RC simultaneously reduces the temperature of the SC during the LT process (to meet both i) and iii) condition).

A practical module, on the other hand, large fraction of the solar energy is utilized in heating the SC by parasitic sub-BG absorption (failure to meet (ii) condition). For instance, 10–90% of sub-BG heating for GaAs, CdTe, CIGS, and silicon SC are measured[31] in various regions including the Urbach tail,[48] absorbing back metal,[49] and passivation layer.[50] The power distribution of practical module is indicated by the colored regions in Figure 1b. The green region represents the efficiency contribution of the solar spectrum, where the cell can generate electricity (P_{out}). The orange represents the absorbed power density below the bandgap of the solar spectrum (P_{sub-BG}). The sky blue region represents cooling power density for the RC (blue line) whose emissivity encompass the entire infrared wavelength range of the atmospheric transmittance window. A silicon SC whose bandgap (λ_g) is at ≈1.17 eV for instance, the heating potential of 228 W m^{-2} is evaluated from the sub-BG photons (orange region, assuming 100% sub-BG absorption). The substantial heat gain, which is nearly half of the cooling

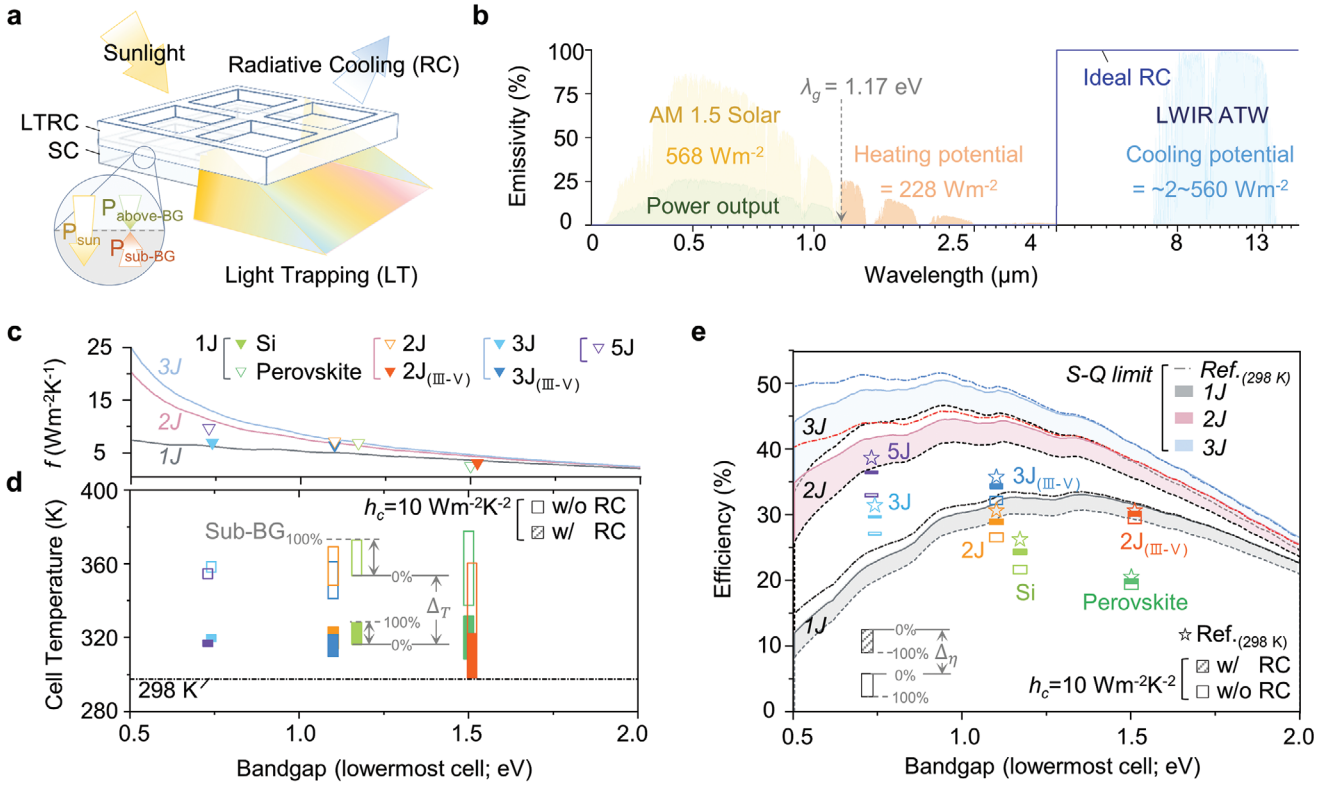

Figure 1. Range of SCs and evaluated cell efficiency with potential cooling/ heating power. The reference SCs are selected based on the presence of both emissivity and temperature coefficient, to calculate cell efficiency and temperature. a) Illustration of RCs which simultaneously radiate heat and trap light. $P_{above-BG}$ is fully absorbed while P_{sub-BG} is fully reflected in ideal SC-RC module. b) Conceptual power distribution in SCs with RC along with the normalized AM 1.5 G solar spectrum and LWIR atmospheric transmittance window (ATW, Mauna key sky condition) model for reference. c) The temperature-efficiency sensitivity factor, *f*, for 1–3 junction SCs. Experimental results are indicated by filled triangle. d) Cell temperature (*T*) of corresponding cells are evaluated as a function of bandgap of the lowermost cell. *T* has a temperature range from 0 (solid) to 100% (dash) of sub-BG absorption for SC with RC (w/ RC, filled bar) and without RC (w/o RC, open bar) cases. e) The SC efficiency (η) range of reference cells[5,15,56–59] as a function of lowermost BG for SC w/ RC (filled bar) and w/o RC (open bar). The η_{Tref} at T_{ref} equals 25 °C (298 K) are also depicted (star). The filled regions indicate evaluated Shockley–Queisser energy conversion efficiency limits (modified S–Q limit, Note S3, Supporting Information) for 1–3 junction (black, red, and blue respectively) from minimum (w/ RC and sub-BG$_{0\%}$) to maximum temperature (w/o RC and sub-BG$_{100\%}$) under global sunlight (AM 1.5 G). The theoretical SQ limit at a cell temperature of 298K is also presented (dashed dot).[3]

potential of 560 W m^{-2} from the RC, is obtained from the sub-BG region.

The net power P_{net} for the practical RC coupled with SC systems is governed by the energy balance equation, which is expressed as:[31,34]

$$P_{net} = P_{rad}(T) - P_{atm}(T_{amb}) - P_{sun} + P_{out}(T) - P_{non-rad}(T_{amb} - T) \quad (1)$$

P_{rad} denotes the power density (W m^{-2}) radiated by the module surface, P_{atm} represents the power absorbed by the atmospheric radiation on the module surface, $P_{non\text{-}rad}$ represents the non-radiative heat transfer (i.e., convection and conduction) between the module and the ambient air or ground.[51,52] The absorbed power density of solar irradiance on the module is denoted by P_{sun}, which includes the heating by parasitic sub-BG absorption (P_{sub-BG}) from the surroundings ($P_{sun} = P_{above-BG} + P_{sub-BG}$). P_{out} represents the electrical power density generated from the SC, which has a positive sign because it does not contribute to heating (Equations S6–S8, Supporting Information). For the system in the steady state, where P_{net} equals zero, the temperature (T) of the module can be evaluated at a given ambient temperature (T_{amb}). (see also Experimental Section, Figure S1, and Note S1, Supporting Information).

3. The Relation between Temperature and Efficiency of the SC

There exists a negative temperature–efficiency (T–η) relation of SC, which is expressed as $\eta(T) = \eta_{T_{ref}} \times [1 - \beta(T - T_{ref})]$, where $\eta_{T_{ref}}$ represents the power conversion efficiency of SC at a reference temperature, T_{ref}, of 25 °C and at a solar radiation flux of 1000 W m^{-2}.[15,53] The temperature coefficient, β, is primarily a material property, implying the degree of decrease in the output power due to the elevated SC temperature, T (Note S2, Supporting Information).[54] In order to provide a better understanding of the concept, the temperature-efficiency sensitivity factor, f, is defined as:

$$f = \eta_{T_{ref}} \times \beta \quad (2)$$

The temperature-efficiency relation can then be written again as:

$$\eta(T) = \eta_{T_{ref}} - f \times (T - T_{ref}) \quad (3)$$

Subsequently, the f for single (1 J, gray line), dual (2 J, pink line), and triple (3 J, sky blue line) junction SCs is calculated from the analytical solution of β[55] and the maximum efficiency (S–Q limit, assuming that all SC recombination is radiative and there is no other extrinsic limitation)[3] for each case presented in Figure 1c. Consequently, the f can be demonstrated to be approximately proportional to the number of junctions, which implies that η degradation is more tendered for 5J SC with the increase in ($T - T_{ref}$), with the lowest λ_g between 0.5–0.75 eV.

The f is then evaluated for several reference cells,[5,15,56–59] indicated by the triangles in Figure 1c. For example, in the cases of the InGaP/GaAs/Ge 3 J SC, which has a λ_g of 1.96/1.52/0.74 eV for each cell, the SC is marked at 0.74 eV (Ge).[58] The f was derived by referring to the values of $\eta_{T_{ref}}$ and β in previous pioneering researches. Note that the referred β was selected as derived from a SC with the same structure (crystalline structure, material, and order of junction, etc.) and $\eta_{T_{ref}}$ as the targeted SCs (Table S1, Supporting Information). A filled triangle in Figure 1c indicated f derived from the experimentally obtained η (fall below S–Q limit due to additional losses, including non-radiative recombination, collection, and electrical losses) and β in this instance. It is observed in each SC that the highest f is obtained from the 5 J SC, which has the largest number of junctions, whose lowest cell has a λ_g of ≈0.73 eV (purple triangle) (Note S2, Supporting Information).[15,59]

The f can be used to determine the SC which exhibits the most sensitive reduction in the electrical performance due to heating. However, the actual T must be calculated because it can slightly increase, possibly resulting in smaller η degradation even for a larger f value. From $\eta(T) = P_{out}(T)/P_{in} \times 100\%$, the electrical power output $P_{out}(T)$ in Equation (1), of the module can be expressed by:[31,32]

$$P_{out}(T) = P_{out}(T_{ref}) - f \times (T - T_{ref}) \quad (4)$$

where P_{in} is the incident solar irradiance of 1000 W m^{-2} and $P_{out}(T_{ref})$ is the electrical power output at reference temperature of 25 °C . Now, at a steady state, both T and η of the practical SC-RC module obtained simultaneously. Considering both RC cooling and sub-BG heating, four possible conditions can be inferred: SC i) with or ii) without RC (w/RC and w/o RC, respectively) and SC heated by iii) 0% or iv) 100% sub-BG absorption (sub-$BG_{0\%}$ and Sub-$BG_{100\%}$, respectively). It is assumed that a 0–100% range of sub-BG absorption contributes to the heating power to consider all the possible situations.

4. Theoretical Analysis for 1, 2, and 3 Junction SCs

Firstly, the SC that is the least vulnerable to sub-BG heating is determined. By applying Equations (1)–(4) for given T_{amb} of 25 °C and at a solar radiation flux of 1000 W m^{-2}, the T and η are obtained. Figure 1d,e illustrate the evaluated T and η versus energy absorption threshold of the lowest bandgap cell for cases i–iv). The non-radiative heat coefficient, h_c, is set as 10 Wm^{-2} K^{-1}, resulting in a wind speed of ≈0.5 m s^{-1} when conductive heat is transferred through the air, and the module is neglected.[31,51] The possible T and η ranges generated by sub-BG heating (from sub-$BG_{0\%}$ to sub-$BG_{100\%}$) are expressed as bars of w/RC (filled bar) and w/o RC (blank bar). The length of the bar depends on the amount of sub-BG heating. The shorter the bar length, the smaller the difference in η between the sub-$BG_{0\%}$ and the sub-$BG_{100\%}$ cases. The length of the bars for w/ RC is shorter than that of w/o RC, which indicates that the SC with an RC design is highly resistant to sub-BG heating. This is because at high T, the outgoing cooling power (i.e., $P_{rad}(T)$) rise only in the case of SC w/RC while the SC w/o RC maintains relatively lower cooling power due to the transparency of semiconductor at infrared region. Thus, the SC w/o RC is more vulnerable to the additional heat gain, i.e., sub-BG heating. In Figure 1d,e, the 5 J (purple filled bar), whose λ_g of lowermost cell is the smallest, has the shortest bar length for

both T and η (≈3 K and 0.2%, respectively; see also Table S2, Supporting Information), indicating that the SC with a higher number of junctions is less susceptible to sub-BG heating.

The cases with the same degree of sub-BG heating are then compared to comprehensively evaluate the RC cooling effect. The T and η differences between w/RC and w/o RC are marked as Δ_T and Δ_η (distance between filled and blank bars) in Figure 1d,e. The effect of RC increases with the increase in the values of Δ_η. The 5 J (purple bars), which has the largest number of junctions, shows the highest Δ_η values for both the sub-$BG_{0\%}$ (distance between solid lines of filled and blank bars) and the sub-$BG_{100\%}$ (distance between dashed lines of filled and blank bar) cases. When comparing the SCs with the same number of junctions, the SC with the lower λ_g presents better RC performance (i.e., larger Δ_η) for both the sub-$BG_{0\%}$ and sub-$BG_{100\%}$ cases. For instance, in the case of 3 J SC, 3 J ($\lambda_g \approx 0.74$ eV) and 3 J $_{(III\text{-}V)}$ ($\lambda_g \approx 1.1$ eV), the Δ_η of the former is calculated to be 2.5%, which is 0.6% higher than the latter for sub-$BG_{0\%}$ case. Therefore, the effect of RC is stronger for a higher number of junctions. In cases where the number of junctions is identical, the RC effect is stronger for a smaller value of λ_g(see Note S4, Supporting Information, for the detailed discussion).

To summarize the section, the MJSC with a low bandgap is the least vulnerable to sub-bandgap heating and shows the highest increase in the efficiency due to radiative cooling. These results quantitatively support the statements made at the beginning of this paper: determining the dependency of RC on the various type of SCs. The effectiveness of RC to SCs is decided from i) how much the temperature of the SC will drop due to RC and ii) how much the dropped temperature due to RC will contribute to the increase in SC efficiency. Since the MJSC with low bandgap absorbs wide solar spectral range, the power of sub-bandgap heating is small which accounts for only a portion of the overall powers in the energy balance equation (Equation (1)). Thus, the cooling power can overwhelm the others so that the RC drops the temperature of MJSC most among other SCs (Answer to (i)). Furthermore, as the MJSC with low bandgap has high value of temperature sensitivity factor f, efficiency drops more significantly compared to other SCs. In other words, η rise is more significant from the T drops than any other SCs (Answer to (ii)). Accordingly, the MJSC with a low bandgap can maintain η better than the other types of SCs at high environmental temperatures when applying the RC technique. This result also holds true for various outdoor conditions when considering non-radiative heat transfer coefficient, h_c, as evaluated in Figure S3, Supporting Information.

5. Design and Fabrication of LTRC

An RC is applied to the MJSC based on the analysis presented in Figure 1. The applied cooler comprises a 2D micro-grating patterned glass, as depicted in the scanning electron microscopy (SEM) images presented in **Figure 2**a (left). The pattern has a period of 8.5 μm, depth of 2 μm, and a duty cycle of 85%. In the proposed design, the grating pattern of the cooler enhances both the radiative cooling and the light-trapping performance. This cooler is termed as the LTRC based on its function, and the cooler without the patterned glass is termed as RC. The following functions are derived from independent operations in the solar spectrum and long-wave infrared (LWIR) region: 1) increase in the solar energy gain by diffracting the glazing sunlight and 2) enhancement of thermal emission by ameliorating thermal emission in the LWIR region. A clear ultraviolet curable adhesive (NOA61, Norland, USA) is used to bond the LTRC and MJSC. The used optical adhesive is clear and transparent for the solar spectrum, hence it barely absorbs the sunlight.[60]

Figure 2a (right) presents the conceptual image of the applied SC, which is composed of $In_{0.5}Ga_{0.5}P$ (0.7 μm), GaAs (3.65 μm), and Ge (150 μm) without anti-reflection coating. Gold metal is meshed on the top side and plated on the bottom side of the MJSC, and sapphire is used as the substrate. Figure 2b,c illustrate the enhanced absorption presented by LTRC when compared to those of common glass (i.e., RC) for the glazing incident angle (i.e., the incident angle of 80°). The absorption layers are changed based on the wavelength, but all the layers of the LTRC on MJSC (MJSC/LTRC) present stronger absorptions than those of bare glass on MJSC (MJSC/RC). Figure 2d presents the total solar absorptions (i.e., P_{Sun}) of the three cells, MJSC/LTRC, MJSC/RC, and MJSC, as a function of the incident angle. Figure S5, Supporting Information, presents the comprehensive simulation results. The solar energy gain is considerably increased, particularly at the glazing angle, owing to the elongated optical path produced by the diffraction of the LTRC. This characteristic increases the amount of energy harvested by the photovoltaic cells throughout the day.

Figure 2e illustrates the absorptivity (or emissivity) spectra of three cells including the solar spectrum and the LWIR region. The spectral results are calculated based on the normal incidence of light. Theoretically, MJSC has almost zero emissivity since semiconductor materials are usually LWIR transparent and since the gold layers perfectly reflect the thermal wavelengths (Figure 2e; gray curve). Although a glass material on the MJSC presents a modest emissivity to the overall cell, a high contrast of the optical constants between the glass and air inevitably generates a loss in the emissivity in the LWIR atmospheric transmittance window regime (Figure 2e; red curve). Conversely, the MJSC/LTRC exhibits reinforced emissivity loss owing to the photonic crystal effect[36] of 2D micro-grating at the scale of thermal wavelengths (Figure 2e; blue curve). 3D simulation results reveal that such emissivity improvement originates from the minimization of strong surface reflection at the interface between air and glass (Figure S4). Furthermore, both the glass and the LTRC constitute an anti-reflection coating on the MJSC in the solar spectrum. However, the MJSC/LTRC absorbs more solar energy than the MJSC/RC as shown in Figure 2e.

Based on these spectral results, the energy balancing Equation (3) is solved for the three cells depicted in Figure 2f,g. The f values are derived through experimental analysis, where $f = 40.6$, 41.12, and 42.72 Wm^{-2} K^{-1} are used for MJSC, MJSC/RC, and MJSC/LTRC respectively. The MJSC exhibits the highest temperature for the h_c values between 1 and 200, as shown in Figure 2f. As explained earlier, η is expected to be the lowest for this sample. For $h_c = 10$ W m^{-2} K^{-1}, the MJSC/LTRC exhibits a higher η value than the other samples in the equilibrium state: MJSC/LTRC, 25.914%; MJSC/RC, 24.812%; MJSC, 23.774% (Figure 2g).

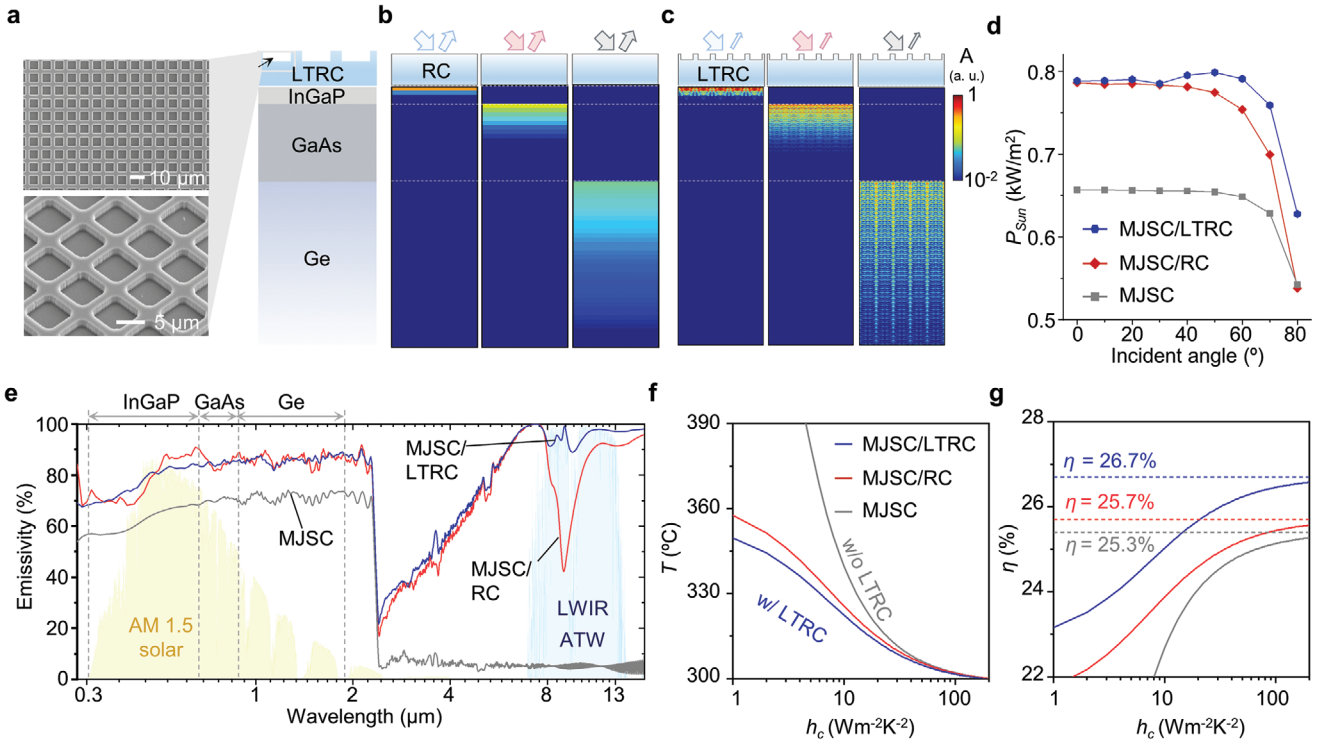

Figure 2. Multi-junction SCs with grating structure which functions for both radiative cooling (RC) and light trapping (LT). a) SEM images for optimized LTRC at top view and bottom (tilted) view. Schematic illustration of multi-junction SC (MJSC) integrated with light trapping RC (LTRC). LTRC on MJSC simultaneously increases thermal radiation and solar gain. b,c) Absorption profiles of MJSC/RC and MJSC/LTRC for three wavelengths (i.e., 430, 750, and 1500 nm) corresponding to absorbed photons in three active layers (i.e., $In_{0.5}Ga_{0.5}P$, GaAs, and Ge), respectively. The incident angle is 70°. d) Calculated solar power absorption (P_{Sun}) based on incident angle for three samples. e) Absorptivity (or emissivity) spectra of only MJSC, MJSC/RC, and MJSC/LTRC. Triple-junction of MJSC absorbs most of the solar spectrum from the wavelength of 0.3 to 1.9 μm. The MJSC/LTRC presents prominent solar absorptivity and enhanced emissivity in long-wave infrared (LWIR, Mauna key sky condition) region. f,g) Calculated T and η of three samples using energy balance with emissivity spectra obtained from (e).

6. Characterization of LTRC in Terms of Radiative Cooling and Light-Trapping

Figure 3a presents a photograph of the fabricated LTRC under direct sunlight. Full-scale wave analyses are used to optimize the LTRC in terms of the cooling performance (Figure S6, Supporting Information). The implementable optimal parameters are derived from the optimization step as follows: depth - 2 μm; period - 8.5 μm, and duty cycle - 75%. The measured spectral features demonstrate that the LTRC has exceptional emissivity in the LWIR region and a transmittance comparable to that of glass in the solar spectrum (Figure 3b). Furthermore, the LTRC presents a higher average emissivity ranging from 8 to 16 μm in the omnidirectional angles (Figure 3c).

A light-trapping effect enhances the photon absorption in the active layers by increasing the light path. The proposed LTRC can also produce a light-trapping effect through diffraction within an almost full solar spectrum. Firstly, the simulation results determine the efficiency and diffracted angle (θ_d) as functions of the wavelength (λ) and incident angle (θ_i) (Figure S7, Supporting Information). These results indicate that higher incident angles considerably refract the incident light (i.e., $\theta_d > 60°$) to present better light-trapping effect; hence, the LTRC integrated cell can present a high solar absorption at oblique incident angles. The diffraction presented by LTRC is experimentally demonstrated under three laser sources with center wavelengths of 450, 532, and 635 nm corresponding to blue, green, and red lights, respectively (Figure 3d). Figure S8, Supporting Information, illustrates the measurement setup and the method used to measure the diffraction angle. The simulation results verify the measured diffracted angles, as shown in Figure S9, Supporting Information. Both the measurement and simulation results indicate that a light with a longer wavelength is crooked with a larger angle than the light with a shorter wavelength, which helps in improving the light-trapping effect (Figure 3e).

7. Opto-Electro-Thermal Energy Analysis of SC-RC Module

The MJSC is then integrated with glass (MJSC/RC) and LTRC (MJSC/LTRC). **Figure 4**a illustrates the power density of the three different samples in the solar spectral range. The MJSC/LTRC exhibits the highest power density in all the solar spectra among the cells. Figure S10, Supporting Information, presents the measured absorptivity spectra of the three cells. The sub-BG absorptivity, ε_g(1.67 μm < λ < 2.5 μm), is measured to be 67.6, 73.6, and 77.2% for the MJSC, MJSC/RC, and MJSC/LTRC respectively.

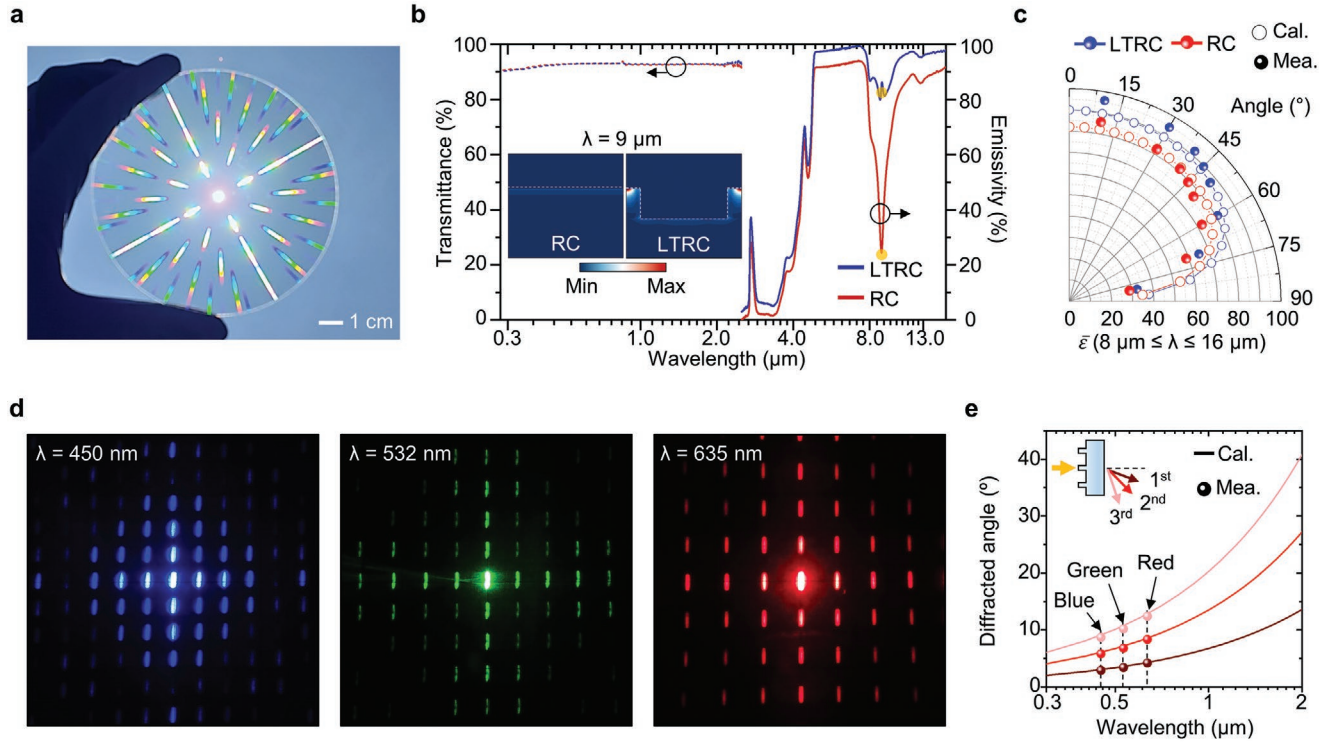

Figure 3. Optical features of LTRC. a) Photograph of LTRC under sunlight. b) Measured transmittance and emissivity spectral features of LTRC (blue) and bare glass (red). Insets depict the absorption profiles of glass and LTRC at wavelength of 9 μm. c) Angular mean emissivity of LTRC (blue) and glass (red) from the wavelength of 8 to 16 μm. Filled and empty circles indicate measured and simulated results, respectively. d) Photographs of three diffracted lights with the center wavelengths of 450, 532, and 635 nm. e) Measured and calculated diffracted angles versus wavelength. Red, blue, and green lines represent 1st, 2nd, and 3rd diffraction.

The stronger absorption presented by MJSC/LTRC in comparison to the others indicates increased electrical power output after mounting, as shown in Figure 4b. Consequently, it indicates the greatest increase in the measured power conversion efficiency (η) for MJSC/LTRC, with 1.32%, as shown in Figure 4c. The $\Delta_\eta (= \eta_{T_{ref}} - \eta(T))$ equals to 1.556% for $h_c = 5$ W m^{-2} K^{-1} and 0.453% for $h_c = 30$ W m^{-2} K^{-1} for the MJSC/LTRC module (Figure S19f, Supporting Information). As tht most powerful RC among others potentially achieves 0.5–2% of $\eta(T)$ compensation from $\eta_{T_{ref}}$ when cell temperature (T) rises, it would like to be said that the increase of 1.3% of $\eta_{T_{ref}}$ is sufficiently efficient. Figure S11, Supporting Information, presents the detailed curves of the current density versus voltage for the others. These measured efficiencies are cross-verified to ensure low uncertainty of measured results (Figures S12, Tables S3 and S4, Supporting Information) based on the SC checklist (see also Note S5, Supporting Information).[61,62]

The cooling power is determined by the power flux in the infrared region, indicating that the larger the P_{rad} (power radiated by the module) with a smaller P_{atm} (power absorbed by the atmosphere), the greater the cooling power. Figure 4d demonstrates that the MJSC/RC and MJSC/LTRC have comparable P_{atm} values (Figure 4d; colored area). However, the latter shows the highest P_{rad}, indicating a superior cooling performance (Figure 4d; colored lines). The spectra of the radiative density are calculated based on the measured emissivity of the three cells (Figure S10b, Supporting Information). The electrical power output (P_{out}) strongly determines the cooling performance in the power analysis because the solar irradiance (P_{sun}) absorbed by the structure is used to produce Pout as well as the heat gain (P_{loss}) (Equations S8, Supporting Information).

Figure 4e presents the aforementioned equation with the variation of cell temperature corresponding to two possible $T - \eta$ sensitivity factors, f (Notes S2 and S3, Supporting Information).[63] It is observed that P_{out} decreases more for a high f (solid line) value than for a low f value, as explained earlier. Figure 4f summarizes the quantitative analysis of the SC-RC coupled systems by demonstrating the correlation between the power density components for P_{sun}, P_{rad}, $P_{non\text{-}rad}$, and P_{atm}. The integrated values of the spectra are presented in Figure 4a,d considering the AM 1.5 G solar spectrum and the atmospheric transmittance window, respectively. In this calculation, T_{amb}, f, and h_c are chosen to be 298 K, 6.94% K^{-1}, and 10 W m^{-2} K^{-1}, respectively. MJSC/LTRC presents the highest cooling power, as indicated qualitatively in Figure 4d. Furthermore, the largest P_{out} value presents the lowest MJSC/LTRC heating effect. As a result, the MJSC/LTRC achieves the lowest temperature, which is 8.8 °C lower than that of MJSC.

8. Outdoor Field Test

Field tests are performed for MJSC, MJSC/RC, and MJSC/LTRC to demonstrate the improvement in the cooling performance and solar energy gain presented by the LTRC. **Figure 5**a,b

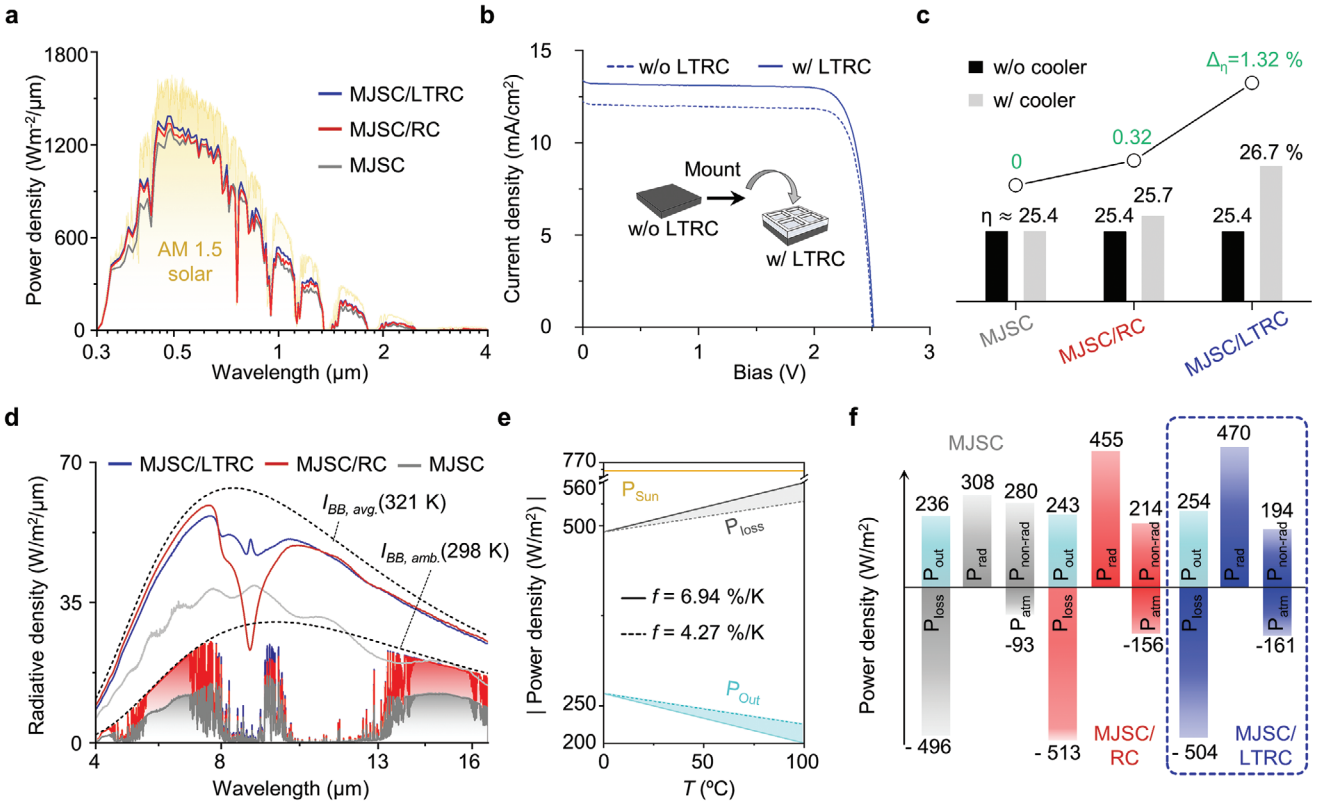

Figure 4. Opto-electro-thermal energy analysis of systems. a) Power density spectra absorbed by the MJSC (gray), MJSC/RC (red) and MJSC/LTRC (blue); normalized AM 1.5 G solar spectrum is provided for reference. The spectra of power density are reconstructed using measured result in Figure S10a, Supporting Information. b) Measured current density-voltage curves of MJSCs before (dashed) and after (solid) mounting the cooler. c) Comparison of measured power conversion efficiency (η) before (black) and after (gray) mounting the cooler with variation of η (green). d) Radiative power densities (solid line; P_{rad}) of the mounted MJSCs and atmospheric emission power density (gray box; P_{atm}) distribution as a function of radiation wavelength; blackbody radiation curves (I_{BB}) for T_{amb} (298 K, $I_{BB, amb.}$) and average temperature of MJSC (53 °C), MJSC/RC (46.4 °C), and MJSC/LTRC (44.2 °C) (321 K, $I_{BB, avg.}$) are provided for reference (dashed). The spectra of radiative density are reconstructed using measured result in Figure S10b Supporting Information. e) Possible MJSC/LTRC electrical power output (P_{Out}) drops by MJSC heating power (P_{loss}) for a range of f. f) Quantitative analysis of the power density components within the radiative cooling system at the equilibrium states.

illustrate the rooftop measurement condition under direct sunlight, to measure the temperatures, open-circuit voltages (V_{oc}), and short-circuit currents (I_{sc}). The measurement setup (acrylic chamber, Figure 5b) is laid on the wooden table with a height of ≈1 m to avoid any heating effect from the ground, as shown in the photograph presented in Figure 5a. Styrofoam boxes are used in each cell for thermal isolation from the bottom of the wooden table. A convection shield is used to analyze the effect of radiative cooling on the cells by minimizing the convection effect. The surface-laminated temperature sensors are attached to the bottom surface of each cell, and electrical wires are connected to the gold plate on the substrate. An air temperature sensor is inserted into the Al box to prevent the self-heating problem, and one side of the air box is open to provide natural air flow.[18] Figure S13, Supporting Information, illustrates the detailed measurement setup. Optical and thermal images of the samples under sunlight are also presented (Figure 5b, top). In the thermal images, only the MJSC presents extremely low temperatures. A high temperature is observed in the case of glass; however, the LTRC exhibits the highest temperature. These ironic results, where the MJSC and MJSC/LTRC show the lowest and highest temperatures, originate from the emissivity difference, not real temperatures. Fundamentally, apparent temperatures from thermographic images are determined by the amount of radiation emitted from an object. Therefore, high temperature in the top of Figure 5b indicates the large amount of thermal emission. In this context, thermal images imply that the LTRC has a near-ideal thermal emission.

The proposed LTRC can simultaneously reduce the cell temperature and increase the cell efficiency, as explained earlier. These theoretical results are verified by measuring the ambient temperatures (T_{air}), T, and V_{OC} for three different days, as shown in Figure 5c, where each value is time-averaged. The V_{OC} is measured to quantitatively analyze the thermal degradation of the cells, which is expressed as a value divided by the maximum V_{OC} value ($V_{OC}/V_{OC,Max}$). For instance, the MJSC/LTRC maintains the highest $V_{OC}/V_{OC,Max}$ under a peak solar intensity I_{solar} of ≈989 Wm^{-2} and a clear sky on Day 2, where the V_{oc} drop is ≈6% of the maximum V_{oc} during measurement. The MJSC/RC and MJSC demonstrate larger V_{oc} drops of ≈7% and 8%, respectively, from the maximum V_{oc}, owing to the cooling effect of the LTRC. It is observed that the MJSC/LTRC achieves the lowest T of ≈47.2 °C, which is 4.7 and 6.1 °C lower than those for the MJSC/RC and MJSC, respectively. Figure 5d presents

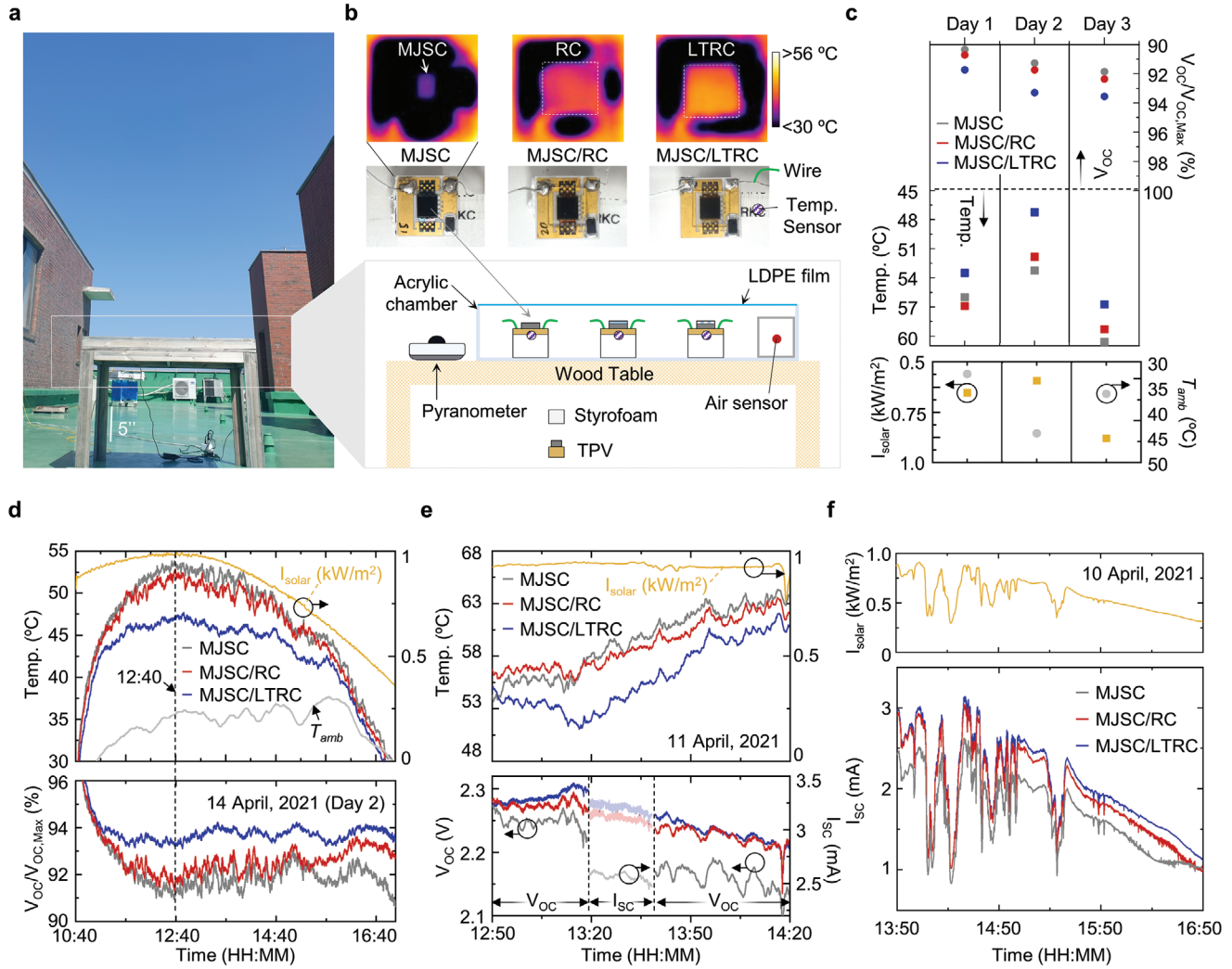

Figure 5. Outdoor field test of cells. a) Photograph and b) (bottom) Schematic illustration of measurement setup. (top) Optical and thermal images of three samples. MJSC exhibits the highest temperature under sunlight among three samples. This indicates that the LTRC strongly emits thermal radiation. c) Measured results of V_{OC} variation and temperature for four days. d) Measured temperatures and V_{OC} variations of three samples during daytime. The temperature drops of MJSC/LTRC are ≈5 °C when compared to that of MJSC/RC. e) Logged data of three samples for temperature, open-circuit voltage (V_{OC}), and short-circuit current (I_{SC}). f) Measured I_{SC} of three samples for daytime. Particularly, MJSC/LTRC shows the highest short-circuit current at the glazing angle of sunlight.

the conditions of Day 2 in detail. The measured results for all the days demonstrate that the MJSC/LTRC maintains the lowest temperature and the highest V_{oc}. Figure S15, Supporting Information, presents the measurement results for the other days. In addition, outdoor field tests without convection shield under the condition of low ambient temperatures are conducted to investigate the cooling capability (S16-S20). The detailed discussion is described in Note S6, Supporting Information.

The measurements are also derived to obtain V_{OC} and I_{SC} alternatively (Figure 5e; bottom), while the temperature is continuously measured (Figure 5e; top). In the temperature results, the MJSC/RC presents a modest temperature drop (≈1 °C) when compared to the MJSC alone. This result can be attributed to the anti-reflection effect of glass, which provides a higher solar gain into the MJSC. Additionally, the parasitic thermal emissivity of the MJSC is one of the reasons for the reduction in the temperature difference with the MJSC/RC. However, the MJSC/LTRC presents an excellent temperature drop of ≈5 °C when compared to the MJSC/RC. These results demonstrate that MJSC/LTRC has the lowest temperature, thereby increasing the V_{OC}. Concurrently, it is proved that the MJSC/LTRC has the highest measured value of I_{SC}, corresponding to an improvement in the photon absorption. Three of the MJSCs present slightly different V_{OC} and J_{SC} before integration with the coolers (i.e., RC and LTRC), as shown in Figure S14, Supporting Information; however, the MJSC for LTRC has the lowest J_{SC} and V_{OC} values before integration. Thus, the enhancement of solar gain is validated by the highest I_{SC} presented by MJSC/LTRC in the outdoor field test.

Figure 5f also demonstrates that the MJSC/LTRC enhances the solar energy gain, particularly at a low solar angle. At a high solar angle (i.e., 13:50), the measured I_{SC} of the MJSC/LTRC is similar to that of the MJSC/RC even though the former is slightly higher than the latter. However, the difference in the

I_{SC} between MJSC/LTRC and MJSC/RC increases at low solar angles (i.e., after 15:50). In cloudy days, both sunlight and outgoing radiation to outer space are blocked by clouds; the heating by sunlight and cooling by thermal radiation does not occur. However, the absolute magnitude of solar absorption exceeds the amount of thermal radiation. Thus, the temperature of SCs steeply decreases when clouds shade the SCs (Figure S17, Supporting Information). These results successfully demonstrate the exceptional cooling and solar energy gain features of the LTRC. Other weather conditions such as relative humidity, wind speed, and outside air temperature are summarized in Table S5, Supporting Information.

9. Conclusion

This study demonstrates the considerable potential of RC in the SC industry by drawing a comparison between various types of SCs. The temperature-efficiency sensitivity factor, *f*, is defined and calculated to provide a better understanding. The MJSC with a low bandgap is observed to present the greatest decrease in η due to the heating (i.e., the largest *f*). Essentially, the MJSC is expected to produce the highest η-compensation effect by the RC. Based on theoretical analysis, a 3 J SC (InGaP/GaAs/Ge) was selected and integrated with the LTRC, presenting a near-unity thermal emission in the LWIR region and improving the solar gain in the solar spectrum. The optical simulations and measurements confirmed the efficient radiative cooling and solar diffraction characteristics, enabling the light-trapping effect. A power analysis was conducted for three different SCs (i.e., MJSC, MJSC/RC, MJSC/LTRC) based on the measured spectrum and efficiency. Consequently, the MJSC/LTRC was confirmed to have the highest electricity generation (P_{out}) and the lowest heat generation (P_{loss}). The outdoor field tests experimentally demonstrated that the MJSC/LTRC presents the lowest cell heating effect to minimize the degradation of the open-circuit voltage and the highest photon absorption owing to the light-trapping effect. Specifically, the quantitative results of MJSC/LTRC are when comparing to those of only MJSC as follows: 1) 6.1 °C cooling of cell temperature, 2) 2% increasing of $V_{OC}/V_{OC,max}$, and 3) 0.5 mA increasing of I_{sc}. The repeated field tests demonstrated the data reliability. This study highlights the major limitations faced by the SC industry, that is, the η of SC modules is lower under practical operating conditions when compared to the standard test conditions. The application of the RC to the SC and the suppression of the parasitic heat are promising solutions in resolving the problems faced in the prediction of the SC energy production. Particularly, the MJSC to which LTRC is applied, is expected to have the highest efficiency under both indoor (i.e., standard test condition) and outdoor conditions. Although a long-term measurement still remains as future work for evaluating service-life, MJSC/LTRC might have a common service lifetime of other SCs because LTRC is based on glass material and easily maintained by washing smooth water periodically.[64] The radiative cooling approach presented in this study is effective especially for the MJSC and also for concentrating photovoltaic cells, which is expected to present a large *f* value owing to its high efficiency ($\eta_{T_{ref}}$). Therefore, the field of RC can be integrated with the SC industry, presenting a new perspective of efficiency control in the external environment.

10. Experimental Section

Solution Methodology for SC Temperature (T) and Efficiency (η): MATLAB was used to investigate the *T* and η from the iteration. The solution procedure for the RC-SC coupled model is illustrated by the flowchart in Figure S1, Supporting Information. The *T* was first assumed as 25 °C and ΔT as 0.02 °C to start the simulation. From the given $\eta_{T_{ref}}$, *f*, and assumed $T(= T_{old} = 25\ °C)$, $P_{out}(T)$ was calculated using Equation (4). From the solution of the energy balance equation (Equation (1)), net power of the system (P_{net}) was estimated. The sign of ΔT is determined according to the sign of P_{net}, and the new value of SC temperature ($T_{new} = T_{old} + \Delta T$) is acquired. The T_{new} was used to calculate the new value of $P_{out}(T_{new})$ using Equation (4). This iterative technique was repeated until the P_{net} of the energy equation become less than 10^{-3} W m^{-2}.[65] Finally, the SC temperature *T* is evaluated, and the SC efficiency $\eta(T)$ is obtained simultaneously from the solution of Equation (3).

Numerical Simulation for Absorption Profiles and Spectral Results: A 3D wave simulation software (DiffractMOD, RSoft Design Group, Synopsys, USA) based on rigorous coupled-wave analysis (RCWA) was used to investigate emissivity spectral results for all samples. In addition, absorption profiles were simulated using the same software. In all simulations, a square grid size of 1 nm was exploited for sufficiently stable calculated results. Moreover, complex refractive indices were considered to achieve an accurate result. The used complex optical constants of SiO_2 were obtained from the literature,[66] and those of other semiconductor materials such as Ge, GaAs, and InGaP were given by library of the software. For Au metal, Drude model was utilized to achieve material dispersion.

Fabrication of LTRC: A clean quartz substrate was prepared, and a 100 nm-thick Cr layer was deposited on the substrate as an etching mask using an electron beam evaporator (KVE-E2000, Korea Vacuum Tech Ltd., Korea). The deposition rate and pressure were ≈1 Å s^{-1} and ≈10^{-6} Torr, respectively. A quartz crystal sensor was used to monitor the deposited thickness in real time. Spin coating was performed after the deposition of Cr using a positive photoresist (PR; AZ5214E, MicroChemicals, Germany) at 4000 rpm for 30 s. The sample was then baked at 90 °C for 60 s as a soft bake step. Subsequently, UV exposure was conducted with a 2D micro-grating mask at a wavelength of 365 nm for 10 s to generate a pattern on the sample. The sample was then developed by immersing a developer (AZ-MIF-300, MicroChemicals, Germany) for 60 s. Hard-baking was also performed at 110 °C for 120 s, and the sample was immersed in a Cr etchant (CR-7, Transene Company Inc., USA) to etch the Cr mask for 1 min. Reactive ion etching (Oxford Instruments, UK) was then applied to the sample for 43 min to etch the groove with a depth of ≈1.7 µm. CF_4 gas was used as an etching gas with a flow of 50 sccm; the working pressure and radio frequency power were 30 mTorr and 100 W, respectively. The sample was then completed by removing the residual Cr layer with a Cr etchant for 15 min.

Structural and Spectral Analyses of the Fabricated Samples: The transmittance spectra were characterized with an integrating sphere over the wavelength range of 280 to 2500 nm using an ultraviolet–visible–near-infrared spectrometer (Lambda 950, Perkin Elmer, Inc., USA). Additionally, the emissivity spectra for mid- and long-wave infrared regions were analyzed using a Fourier transform infrared spectrometer (VERTEX 70v, Bruker, USA) with an Au-coated integrating sphere. The emissivity spectra were evaluated from 100 – reflectivity – transmittance measurements. Structural analyses were also conducted by using SEM (SEM; S-4700, Hitachi Hi-Tech, Japan).

Integration of Solar Windows with MJSCs: Triple-junction photovoltaics composed of 0.7 µm thick $In_{0.5}Ga_{0.5}P$ and 3.65 µm of GaAs on 150 µm of a p-type Ge substrate with three different bandgap energies (i.e., 1.86 eV of InGaP/1.42 eV of GaAs/0.67 eV of Ge). The deposited AlInP window layer had a thickness of 30 nm. TiO_2 (50 nm)/Al_2O_3 (50 nm) was coated

on top of the SC as an anti-reflective layer (Solapoint Co. Ltd, China). The active area is 5.5 mm by 5.5 mm.

The solar windows were cut to a size of 1 cm × 1 cm using a dicing machine to completely cover the active area. The windows were cleaned with acetone, isopropyl alcohol, and deionized water before mounting the solar windows on the MJSCs. The integration of glass and LTRC with MJSC was performed using a UV-curable optical adhesive (NOA61, Norland, USA) at a wavelength of 365 nm for 2 min. After UV curing, the cells were baked to harden the bonding using a convective oven at 60 °C for 24 h.

Field Tests of Mounted Cells: For field tests, the electrical wires were soldered to the Au-coated substrate of the sub-receiver module. A solder paste with Sn 62%, Pb 36.8%, and Ag 0.4% was used for this process. The Styrofoam thermal insulation blocks were also prepared with the same size as that of the sub-receiver module. Double-sided thermal conductive tapes were laminated on the thermal insulation blocks, and temperature sensors (ST-50, RKC Instrument Inc., Japan) were placed on these layers. The sub-receiver modules were placed on a tape and a temperature sensor. The modules on the thermal insulation blocks were positioned on the bottom surface of the pre-fabricated acrylic chamber. The temperatures and voltage/current were logged using two data loggers (GL840, Graphtec Corporation, Japan and OM-CP-OCTPRO, Omega Engineering, USA). An ambient air box covered by Al foil was placed and the air sensor was inserted into the ambient air box to measure the air temperature in the chamber. Low-density polyethylene (LDPE) films were covered on an acrylic chamber to suppress the convection effect. A pyranometer (CMP6, Kipp & Zonen, Netherlands) was placed next to the acrylic chamber.

Supporting Information

Supporting Information is available from the Wiley Online Library or from the author.

Acknowledgements

This work was supported by the National Research Foundation of Korea (NRF-2021R1C1C2013605/2020R1A2C2004983/2018M3D1A1058997/2021M3H4A1A04086552) and by the GIST Research Institute (GRI) grant funded by the GIST in 2021. Also, this work was supported by the Korea Institute of Energy Technology Evaluation and Planning (KETEP) and the Ministry of Trade, Industry & Energy (MOTIE) of the Republic of Korea (No. 20183010014310).

Conflict of Interest

The authors declare no conflict of interest.

Data Availability Statement

The data that support the findings of this study are available from the corresponding author upon reasonable request.

Keywords

multi-junction solar cells, radiative cooling, radiative cooler-integrated solar cells, thermal management

Received: October 19, 2021
Revised: November 30, 2021
Published online:

[1] A. Polman, M. Knight, E. C. Garnett, B. Ehrler, W. C. Sinke, *Science* **2016**, *352*.
[2] K. J. Lee, J.-W. Min, B. Turedi, A. Y. Alsalloum, J.-H. Min, Y. J. Kim, Y. J. Yoo, S. Oh, N. Cho, R. C. Subedi, *ACS Energy Lett.* **2020**, *5*, 3295.
[3] M. A. Green, S. P. Bremner, *Nat. Mater.* **2017**, *16*, 23.
[4] D. P. McMeekin, S. Mahesh, N. K. Noel, M. T. Klug, J. Lim, J. H. Warby, J. M. Ball, L. M. Herz, M. B. Johnston, H. J. Snaith, *Joule* **2019**, *3*, 387.
[5] B. M. Kayes, L. Zhang, R. Twist, I.-K. Ding, G. S. Higashi, *IEEE J. Photovoltaics* **2014**, *4*, 729.
[6] S. Mokkapati, F. Beck, A. Polman, K. Catchpole, *Appl. Phys. Lett.* **2009**, *95*, 053115.
[7] D. H. Wang, D.-G. Choi, K.-J. Lee, J.-H. Jeong, S. H. Jeon, O. O. Park, J. H. Park, *Org. Electron.* **2010**, *11*, 285.
[8] C. Cho, H. Kim, S. Jeong, S.-W. Baek, J.-W. Seo, D. Han, K. Kim, Y. Park, S. Yoo, J.-Y. Lee, *Sol. Energy Mater. Sol. Cells* **2013**, *115*, 36.
[9] Z. Hu, J. Zhang, Y. Zhao, *J. Appl. Phys.* **2012**, *111*, 104516.
[10] H. A. Atwater, A. Polman, *Materials for Sustainable Energy: a Collection of Peer-Reviewed Research and Review Articles from Nature Publishing Group*, World Scientific, Singapore **2011**, p. 1.
[11] Z. Tang, W. Tress, O. Inganäs, *Mater. Today* **2014**, *17*, 389.
[12] H. Gonome, T. Hirai, B. J. Lee, M. Kashiwagi, *Appl. Phys. Lett.* **2021**, *119*, 133903.
[13] S. Pillai, K. Catchpole, T. Trupke, M. Green, *J. Appl. Phys.* **2007**, *101*, 093105.
[14] A. Sachenko, V. Kostylyov, I. Sokolovskyi, M. Evstigneev, *IEEE J. Photovoltaics* **2019**, *10*, 63.
[15] O. Dupré, R. Vaillon, M. A. Green, *Sol. Energy Mater. Sol. Cells* **2015**, *140*, 92.
[16] A. P. Raman, M. Abou Anoma, L. Zhu, E. Rephaeli, S. Fan, *Nature* **2014**, *515*, 540.
[17] J. Mandal, Y. Fu, A. C. Overvig, M. Jia, K. Sun, N. N. Shi, H. Zhou, X. Xiao, N. Yu, Y. Yang, *Science* **2018**, *362*, 315.
[18] S.-Y. Heo, G. J. Lee, Y. J. Kim, S. Ishii, M. S. Kim, T. J. Seok, B. J. Lee, H. Lee, Y. M. Song, *Sci. Adv.* **2020**, *6*, eabb1906.
[19] N. N. Shi, C.-C. Tsai, F. Camino, G. D. Bernard, N. Yu, R. Wehner, *Science* **2015**, *349*, 298.
[20] P.-C. Hsu, A. Y. Song, P. B. Catrysse, C. Liu, Y. Peng, J. Xie, S. Fan, Y. Cui, *Science* **2016**, *353*, 1019.
[21] T. Li, Y. Zhai, S. He, W. Gan, Z. Wei, M. Heidarinejad, D. Dalgo, R. Mi, X. Zhao, J. Song, *Science* **2019**, *364*, 760.
[22] A. Leroy, B. Bhatia, C. C. Kelsall, A. Castillejo-Cuberos, M. Di Capua H, L. Zhao, L. Zhang, A. Guzman, E. Wang, *Sci. Adv.* **2019**, *5*, eaat9480.
[23] L. Zhou, H. Song, J. Liang, M. Singer, M. Zhou, E. Stegenburgs, N. Zhang, C. Xu, T. Ng, Z. Yu, *Nat. Sustain.* **2019**, *2*, 718.
[24] D.-H. Kim, G. J. Lee, S.-Y. Heo, S. Son, K. M. Kang, H. Lee, Y. M. Song, *Opt. Express* **2021**, *29*, 31364.
[25] M. H. Kang, G. J. Lee, J. H. Lee, M. S. Kim, Z. Yan, J.-W. Jeong, Y. M. Song, *Adv. Sci.* **2020**, *8*, 2004885.
[26] M. Kim, D. Lee, S. Son, Y. Yang, H. Lee, J. Rho, *Adv. Opt. Mater.* **2021**, *9*, 2002226.
[27] D. Lee, M. Go, S. Son, M. Kim, T. Badloe, H. Lee, J. K. Kim, J. Rho, *Nano Energy* **2021**, *79*, 105426.
[28] Z. Chen, L. Zhu, W. Li, S. Fan, *Joule* **2019**, *3*, 101.
[29] Y. Lu, Z. Chen, L. Ai, X. Zhang, J. Zhang, J. Li, W. Wang, R. Tan, N. Dai, W. Song, *Sol. RRL* **2017**, *1*, 1700084.
[30] G. Perrakis, A. C. Tasolamprou, G. Kenanakis, E. N. Economou, S. Tzortzakis, M. Kafesaki, *Sci. Rep.* **2021**, *11*, 11552.
[31] X. Sun, T. J. Silverman, Z. Zhou, M. R. Khan, P. Bermel, M. A. Alam, *IEEE J. Photovoltaics* **2017**, *7*, 566.
[32] Z. Zhang, K. Chen, S. Fan, Z. Chen, *Opt. Express* **2021**, *29*, 27554.
[33] A. Shang, X. Li, *Adv. Mater.* **2017**, *29*, 1603492.
[34] Y. An, C. Sheng, X. Li, *Nanoscale* **2019**, *11*, 17073.
[35] W. Li, Y. Shi, K. Chen, L. Zhu, S. Fan, *ACS Photonics* **2017**, *4*, 774.

[36] L. Zhu, A. P. Raman, S. Fan, *Proc. Natl. Acad. Sci. USA* **2015**, *112*, 12282.
[37] S. Lin, L. Ai, J. Zhang, T. Bu, H. Li, F. Huang, J. Zhang, Y. Lu, W. Song, *Sol. Energy Mater. Sol. Cells* **2019**, *203*, 110135.
[38] G. Perrakis, A. C. Tasolamprou, G. Kenanakis, E. N. Economou, S. Tzortzakis, M. Kafesaki, *Opt. Express* **2020**, *28*, 18548.
[39] B. Zhao, M. Hu, X. Ao, G. Pei, *Sol. Energy* **2018**, *176*, 248.
[40] Z. Wang, D. Kortge, J. Zhu, Z. Zhou, H. Torsina, C. Lee, P. Bermel, *Joule* **2020**, *4*, 2702.
[41] Z. Zhou, Z. Wang, P. Bermel, *Opt. Express* **2019**, *27*, A404.
[42] B. K. Mahadevan, S. Naghibi, F. Kargar, A. A. Balandin, *C* **2020**, *6*, 2.
[43] P. Gupta, Y. Kim, J. Im, G. Kang, A. M. Urbas, K. Kim, *ACS Appl. Energy Mater.* **2021**, *4*, 9304.
[44] S. Orfanidis, D. Ramaccia, A. Toscano, *Electromagnetic Waves and Antennas*, Rutgers Univ., Piscataway, NJ, USA **2008**.
[45] O. Ilic, P. Bermel, G. Chen, J. D. Joannopoulos, I. Celanovic, M. Soljačić, *Nat. Nanotechnol.* **2016**, *11*, 320.
[46] T. Hebrink, presented at *2009 34th IEEE Photovoltaic Specialists Conference (PVSC)*, IEEE, Piscataway, NJ **2009**.
[47] T. Hebrink, *Third Generation Photovoltaics*, Vol. *39* (Ed. V. Fthenakis), Intech, **2012**.
[48] S. John, C. Soukoulis, M. H. Cohen, E. Economou, *Phys. Rev. Lett.* **1986**, *57*, 1777.
[49] Z. C. Holman, M. Filipič, B. Lipovšek, S. De Wolf, F. Smole, M. Topič, C. Ballif, *Sol. Energy Mater. Sol. Cells* **2014**, *120*, 426.
[50] R. Santbergen, R. C. van Zolingen, *Sol. Energy Mater. Sol. Cells* **2008**, *92*, 432.
[51] D. Zhao, A. Aili, Y. Zhai, J. Lu, D. Kidd, G. Tan, X. Yin, R. Yang, *Joule* **2019**, *3*, 111.
[52] J. Mandal, Y. Yang, N. Yu, A. P. Raman, *Joule* **2020**, *4*, 1350.
[53] D. Evans, *Sol. Energy* **1981**, *27*, 555.
[54] E. Skoplaki, J. A. Palyvos, *Sol. Energy* **2009**, *83*, 614.
[55] S. Ponce-Alcántara, J. P. Connolly, G. Sánchez, J. M. Miguez, V. Hoffmann, R. Ordás, *Energy Procedia* **2014**, *55*, 578.
[56] K. Yamamoto, K. Yoshikawa, H. Uzu, D. Adachi, *Jpn. J. Appl. Phys.* **2018**, *57*, 08RB20.
[57] M. Mousa, M. M. Salah, F. Z. Amer, A. Saeed, R. I. Mubarak, presented at *2020 2nd International Conference on Smart Power & Internet Energy Systems (SPIES)*, IEEE, Piscataway, NJ **2020**.
[58] M. Yamaguchi, T. Masuda, K. Araki, Y. Ota, K. Nishioka, T. Takamoto, C. Thiel, A. Tsakalidis, A. Jaeger-Waldau, K. Okumura, A. Satou, T. Nakado, K. Yamada, Y. Zushi, T. Tanimoto, K. Nakamura, R. Ozaki, N. Kojima, Y. Ohshita, *J. Phys. D: Appl. Phys.* **2021**, *54*, 504002.
[59] P. Chiu, D. Law, R. Woo, S. Singer, D. Bhusari, W. Hong, A. Zakaria, J. Boisvert, S. Mesropian, R. King, presented at *2014 IEEE 40th Photovoltaic Specialist Conference (PVSC)*, IEEE, Piscataway, NJ **2014**.
[60] https://www.norlandprod.com/adhesives/NOA%2061.html, (Accessed: November 2021).
[61] Y. J. Kim, Y. J. Yoo, D. E. Yoo, D. W. Lee, M. S. Kim, H. J. Jang, Y.-C. Kim, J.-H. Jang, I. S. Kang, Y. M. Song, *ACS Appl. Mater. Interfaces* **2019**, *11*, 36020.
[62] J. A. Christians, J. S. Manser, P. V. Kamat, *J. Phys. Chem* **2015**, *6*, 5.
[63] V. S. Kalinovsky, E. V. Kontrosh, P. A. Dmitriev, P. V. Pokrovsky, A. V. Chekalin, V. M. Andreev, presented at *AIP Conference Proceedings*, College Park, MD **2014**.
[64] R. Kitamura, L. Pilon, M. Jonasz, *Appl. Opt.* **2007**, *46*, 8118.
[65] E. M. Abo-Zahhad, S. Ookawara, A. Radwan, A. El-Shazly, M. El-Kady, M. F. Esmail, *Appl. Therm. Eng.* **2020**, *164*, 114497.
[66] G. Sahoo, G. Mishra, *Opt. Quantum Electron.* **2016**, *48*, 420.